Asian Journal of Chemistry; Vol. 37, No. 1 (2025), 155-165

ASIAN JOURNAL OF CHEMISTRY

https://doi.org/10.14233/ajchem.2025.32931

Structural, Morphological and Electrochemical Studies of Synthesized $BaCuTiO_3$ Doped $NiTiO_3$ Nanocomposites for Energy Storage Application

A. Thulasi[1], N.Y. Sreedhar[1,*], S. Himagirish Kumar[2], Karumanchi Susmitha[1], V. Manjunath[3], N.V. Srihari[4], D. Sai Vinathi[5] and V. Thangaraj[6]

[1]Electroanalytical Lab, Department of Chemistry, Sri Venkateswara University, Tirupati-517502, India
[2]Department of Chemistry, Sri Padmavati Women's University, Tirupati-517502, India
[3]Department of Physics, Sri Padmavati Women's University, Tirupati-517502, India
[4]Department of Physics, TRR Government Degree College, Kandukur-523105, India
[5]DST-CURIE Center, Sri Padmavati Women's University, Tirupati-517502, India
[6]Department of Chemistry, University College of Engineering (BIT Campus), Anna University, Tiruchirappalli-620024, India

*Corresponding author: E-mail: sreedhar_ny@rediffmail.com

Received: 21 October 2024; *Accepted*: 12 December 2024; *Published online*: 31 December 2024; AJC-21863

This research explores the development of $Ba_{0.8}Cu_{0.2}TiO_3$ and $NiTiO_3$ nanocomposites for use in high-performance flexible piezoelectric energy harvesters (FPEHs). This study aims to address the brittleness of traditional piezoceramics by developing flexible nanocomposites that are compatible with wearable electronics. The nanocomposites were synthesized and characterized using various techniques including X-ray diffraction (XRD), field emission scanning electron microscopy (FESEM), energy-dispersive X-ray spectroscopy (EDS), Fourier-transform infrared spectroscopy (FTIR), ultraviolet-visible spectroscopy (UV-Vis), photoluminescence (PL), vibrating sample magnetometry (VSM) and X-ray photoelectron spectroscopy (XPS), cyclic voltammetry (C-V) measurements were employed to evaluate the electrical properties, while piezoelectric modeling and various circuit designs were explored to optimize energy efficiency. The results demonstrate that the addition of $NiTiO_3$ to $Ba_{0.8}Cu_{0.2}TiO_3$ alters the electrical and magnetic properties of the composite, enhancing its suitability for energy storage applications. The energy storage applications of the nanocomposites were evaluated by measuring output voltage, stored energy, open-circuit voltage and short-circuit current. These findings indicated that $Ba_{0.8}Cu_{0.2}TiO_3$-$NiTiO_3$ nanocomposites are the promising materials for flexible piezoelectric energy harvesters, offering improved mechanical flexibility, energy conversion efficiency and environmental stability. This work contributes to the advancement of sustainable energy solutions for powering low-power electronics and portable devices.

Keywords: Piezoelectrics, Nanocomposites, Electromechanical coefficient, Wearable energy harvesters, Open circuit voltage.

INTRODUCTION

Sustainable energy sources are crucial for the continued operation of such micro-devices, which have become increasingly significant over the past few decades due to the invention of smart, lightweight, small electronic devices that run on low power. In recent years, there has been a great deal of research on the potential of energy harvesters based on piezoelectricity from mechanical vibration in energy technologies [1-6]. One of the most practical ways to harvest energy is through the use of piezoelectric materials, which may be used to capture energy from even the erratic ambient vibrations found in nearby systems and structures. Likewise, the energy generated by these devices is not consistent enough to be used directly as a power source, therefore a storage element like a capacitor or battery is usually needed. Because piezoelectric polymers are mechanically flexible and can tolerate high strain, they are a preferable option for piezoelectric energy harvesting applications. In addition, despite their low power density, they produce adequate voltage and have a maximum functional field strength, which allows them to withstand higher driving fields. Furthermore, they are less expensive to fabricate and require less time to process than ceramic-based composites [7,8]. Owing to their multifaceted and distinctive properties, transition metal oxide nanoparticles

have drawn a lot of attention from researchers in recent years, leading to a surge in the manufacture of nanostructured materials [9,10]. Because of their exceptional optical, mechanical, chemical, electrical and piezoelectric properties, $Ba_{0.8}Cu_{0.2}TiO_3$ and $NiTiO_3$ (BCT-NTO) nanocomposite are a popular topic for research.

The high-power density, high operating voltage, low leakage current and quick charging and discharging times of electrostatic capacitors have drawn a lot of attention from researchers nowadays. Thus, it is evident that the enhanced energy density of dielectric capacitors may lead to the development of more compact electronic storage devices capable of substituting batteries or supercapacitors. To reduce unintended energy loss brought on by the power management circuit in between, they can also promote the integration of the energy harvester with a storage device. Various fabrication techniques, including directional solidification, sintering and controlled precipitation, have been utilized to synthesize (BCT-NTO) composites. The synthesis method plays a crucial role in influencing the ferroelectric and ferromagnetic properties of these composites, both in bulk and thin films and is essential for achieving a high magnetoelectric (ME) effect. By fine-tuning the stoichiometry and synthesis parameters, the magnetic, electrical and mechanical properties of ME composites can be customized. Research indicates that increasing the ferrite content enhances conductivity due to leakage currents from the ferrite phase's low resistivity, while also improving elastic interactions. However, this increase can lead to higher porosity, which negatively impacts the dielectric constant, thereby weakening the ME signal. Strong mechanical coupling between grains is vital for optimal performance, which can be achieved through optimized sintering at elevated temperatures and by maintaining small grain sizes to ensure robust grain-to-grain interfaces. Notwithstanding these advantages, elevated synthesis temperatures may induce undesirable chemical interactions between the BCT and NTO regions, resulting in the development of impurities that might substantially impact the characteristics of material [11-15].

The ferroelectric behaviour in these systems arises from mechanisms such as lone-pair electron effects and octahedral distortion, whereas magnetism is attributed to unpaired electron spins in partially filled *d*-orbitals. Single-phase multiferroics are rare due to the inherent conflict between ferroelectricity, which requires empty *d*-subshells and magnetism, which results from partially filled *d*-subshells. However, engineered multiferroics that combine distinct ferroelectric and ferromagnetic phases offer a solution, allowing for tunable properties through the coupling between these behaviours. A number of piezoelectric materials have been studied recently; of these, BCT and NTO are thought to be promising options for energy harvesting due to their superior piezoelectric qualities (high piezoelectric charge constant, d_{33}) and flexibility, respectively. BCT and NTO nanocomposites have been chosen for this investigation and XRD, FESEM, EDS, FTIR, UV-Vis, PL, CV, VSM and XPS are used to evaluate the microstructural, optical characteristics, morphologies and phases of the generated nanoparticles. It was found that the addition of NTO and BCT can modify the conducting and magnetic characteristics of pure $Ba_{0.8}Cu_{0.2}TiO_3$ for use in future industrial processes.

EXPERIMENTAL

Most of the chemicals and reagents were procured from Sigma-Aldrich, USA and used as such.

Synthesis of nanocomposite: The starting materials for the synthesis of $(1-x)(Ba_{0.8}Cu_{0.2}TiO_3) + (x)(NiTiO_3)$ ($x = 0.2$, 0.4, 0.6 and 0.8)/BCT-NTO nanocomposites were chosen as barium nitrate [$Ba(NO_3)_2$, 99.8%], copper nitrate [$Cu(NO)_2{\cdot}3H_2O$, 99.8%], nickel nitrate [$Ni(NO_3)_2{\cdot}6H_2O$, 99.8%] and titanium dioxide [TiO_2, 99.9%]. As the catalyst and solvent in the hydrothermal reaction, NaOH pellets and their aqueous solution were also employed.

Working electrode preparation: Initially, $(x)(NiTiO_3) + (1-x)(Ba_{0.8}Cu_{0.2}TiO_3)$ was prepared as the stoichiometric ratio for BCT-NTO nanocomposites ($x = 0.2$, 0.4, 0.6 and 0.8). The raw components (in nitrate form) were mixed after being weighed. The nitrate components were then dissolved in distilled water and then the combined solution was maintained on a 500 rpm magnetic stirrer. Meanwhile, drops of NaOH aqueous solution were gradually added to the nitrate solution. The solution turned into white colour after being stirred for 2 h and then stored in a stainless-steel autoclave. The hydrothermal reaction was carried out in oven for 8 h at 160 ºC. Finally, the oven was cooled to normal temperature once the reaction was completed.

Fabrication of $Ba_{0.8}Cu_{0.2}TiO_3$-$NiTiO_3$ (BCT-NTO) nanocomposite: The sample washed thoroughly until the pH becomes netural. The powder sample was then dried in a hot air oven for 2 h at 60 ºC for 15 min, dry BCT-NTO nanopowder was ground in an agate mortar to obtain uniform powder particles.

Characterization: The Bruker D8-advanced diffractometer was utilized to record XRD patterns. At room temperature, the optical absorbance spectra were captured using a UV-visible JASCO V-670 spectrophotometer. Morphology and particle size studies were performed with TEM on the JEM 2200FS JEOL and FESEM on the FEI Nova NanoSEM 450. Binding energies were measured using X-ray photoelectron spectroscopy with PHI5000 Versaprobe III. Magnetic properties were examined using the quantum design physical property measuring system (PPMS) D292.

Electrochemical characterization: BCT-NTO composite materials were frequently assessed electrochemically utilizing galvanostatic charge/discharge curves and cyclic voltammetry. The following are the standard formulas used to evaluate different electrochemical properties. The galvanostatic charged-discharge curves are used to calculate specific capacitance.

$$Cs = \frac{It}{m\Delta V}$$

Computation of energy and power densities of the composite material: The energy density and power density of the composite material are calculated as follows:

$$\text{Energy density (E)} = \frac{CV^2}{2}$$

$$\text{Power density (P)} = E/\Delta t$$

where V is the cell voltage in volts; P is the average power density (W kg^{-1}); Δt is the discharge time (s) and E is the energy density (Wh kg^{-1}).

RESULTS AND DISCUSSION

Powder X-ray diffraction (P-XRD) studies: The XRD patterns investigation was employed for the structural analysis of BCT-NTO nanocomposites. The BCT-NTO1 nanocomposite shows peaks of reflections from planes 2θ values of 101° (21.9), 101° (25.1), 250° (31.2), 250° (39.5), 200° (44.8), 211° (55.7), 220° (65.4) and 311° (74.4), respectively. BCT-NTO1 (0.2) shows a high intense peak at 2θ = 31.2° and low intense peak at 2θ = 74.4° corresponding to the 201 and 311 lattice space [16]. The BCT-NTO2 at 2θ depicts values of 101° (21.9), 101° (25.3), 250° (31.3), 250° (38.5), 200° (44.5), 211° (55.7), 220° (65.4) and 311° (74.2), respectively. The BCT-NTO-3 and 4 also similar to BCT-NTO1 and 2 values depicting a high intense peak approximately at 2θ = 31.2° and low intense peak at 2θ = 74.4° corresponding to the 200 and 311 lattice space, respectively (JPCDS: 01-073-1764) (Fig. 1). The crystallinity was increases with increasing the concentrations of the sample. The crystallite sizes of all phases in BCT-NTO1-4 (x = 0.2. 0.4, 0.6 and 0.8) samples were calculated using Scherrer'sequation [17]:

$$d = \frac{k\lambda}{B\cos\theta}$$

where d = crystallite size, k = constant of 0.9, λ t= X-ray wavelength which is 1.5049 Å, θ = Bragg's angle (°) and B = full width at half maximum (FWHM) of the peak. The (101), (100) and (104) reflection peaks were used for crystallite size calculations. The XRD peaks confirmed the crystalline nature BCT-NTO as no additional peaks other than BCT-NTO were observed, supporting successful synthesis of BCT-NTO nanocomposites. The XRD patterns of the nanocomposites containing BCT-NTO exhibited exceptional purity, with no additional minor peaks or extraneous components detected, indicating a high degree of crystallinity. The XRD analysis also showed

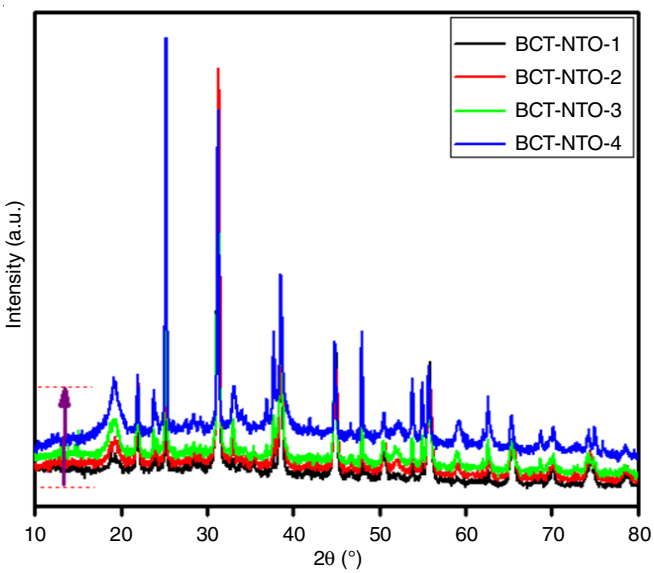

Fig. 1. XRD spectra of $BaCuTiO_3$ doped $NiTiO_3$ nanocomposites (x = 0.2, 0.4, 0.6 and 0.8)

that the R-O and O-T phase transitions occurred near -30 ºC, with the domain structure and the O-T phase transition playing a crucial role in influencing the piezoelectric behaviour. This phase transition contributed to a superior piezoelectric response in the composites compared to pure polymer.

Morphological analysis: TEM and FESEM were used to examine the surface morphology of BCT-NTO nanocomposites. Fig. 2 displays the FESEM images of the BCT-NTO nanocomposites. It can be observed from Fig. 2 that there is significant grain development for every composition. Considering that the grains with x = 0.4 content are obviously larger than the grains of x = 0.2 and 0.6. Furthermore, the morphology of the compositions with x = 0.2, 0.4 and 0.6 is nearly the same, indicating that more irregularly shaped grains are frequently found. On the other hand, the morphology slightly changes quite at x = 0.8. Consequently, this suggests that there is a morphological change from the development of irregularly shaped grains to nearly sharp platelet-like grains. As a result, it is comparable to the structural transition which is already discussed in the XRD studies section from cubic to mixed phases.

Nonetheless, the linear intercept approach was used to calculate the average grain size (Ga = 3L/2MN) [18,19]. The Ga values observed to be changing between 57 and 18 nm (Table-1), thereby confirmed the existence of nano organized. Fig. 3 shows the TEM images of the BCT-NTO nanocomposites employed in this investigation in the 100 nm region. Each BCT nanoparticle has an essentially platelet-like morphology and a particle size of 24-73 nm. The shortage of clustered particles in TEM images is ascribed to the magnetic interactions induced by the presence of copper among the nanoparticles [20]. It follows that the obtained particle sizes are nearly in agreement with the reported grain sizes for all BCT-NTO nanoparticle compositions.

TABLE-1
STRUCTURAL AND PHYSICAL DATA OF $BaCuTiO_3$ DOPED $NiTiO_3$ NANOCOMPOSITES (x = 0.2, 0.4, 0.6 and 0.8)

x	Pos. (°2θ)	Height (cts)	FWHM left (°2θ)	d-spacing (Å)	Rel. int. (%)
0.2	12.1765	35.03	0.1430	7.26283	1.27
0.4	19.2552	145.77	0.4930	4.60584	6.39
0.6	21.9087	361.61	0.2824	4.05363	19.95
0.8	12.6821	40.07	0.0738	6.97442	1.73

FT-IR studies: In the FTIR analysis of $BaCuTiO_3$-$NiTiO_3$ nanoparticle composites with varying compositions (0.2, 0.4, 0.6, 0.8), a comparison of the spectra reveals critical insights into the structural characteristics. The FTIR transmittance spectra of the BCT-NTO nanocomposites were recorded in the range of 4000 to 400 cm^{-1} (Fig. 4). As the $NiTiO_3$ content increases from 0.2 to 0.8, there is a clear shift in the peak position and intensity of the bands related to Ba-O and Cu-O bonds, indicating alterations in lattice environment and bond strength. In 520-400 cm^{-1} range, two types of metal oxide (M-O) stretching vibrations appeared, which is the characteristic peaks of the perovskite BCT-NTO material. Around 510 cm^{-1} of thin transmittance band was observed and the presence of Ba-O,

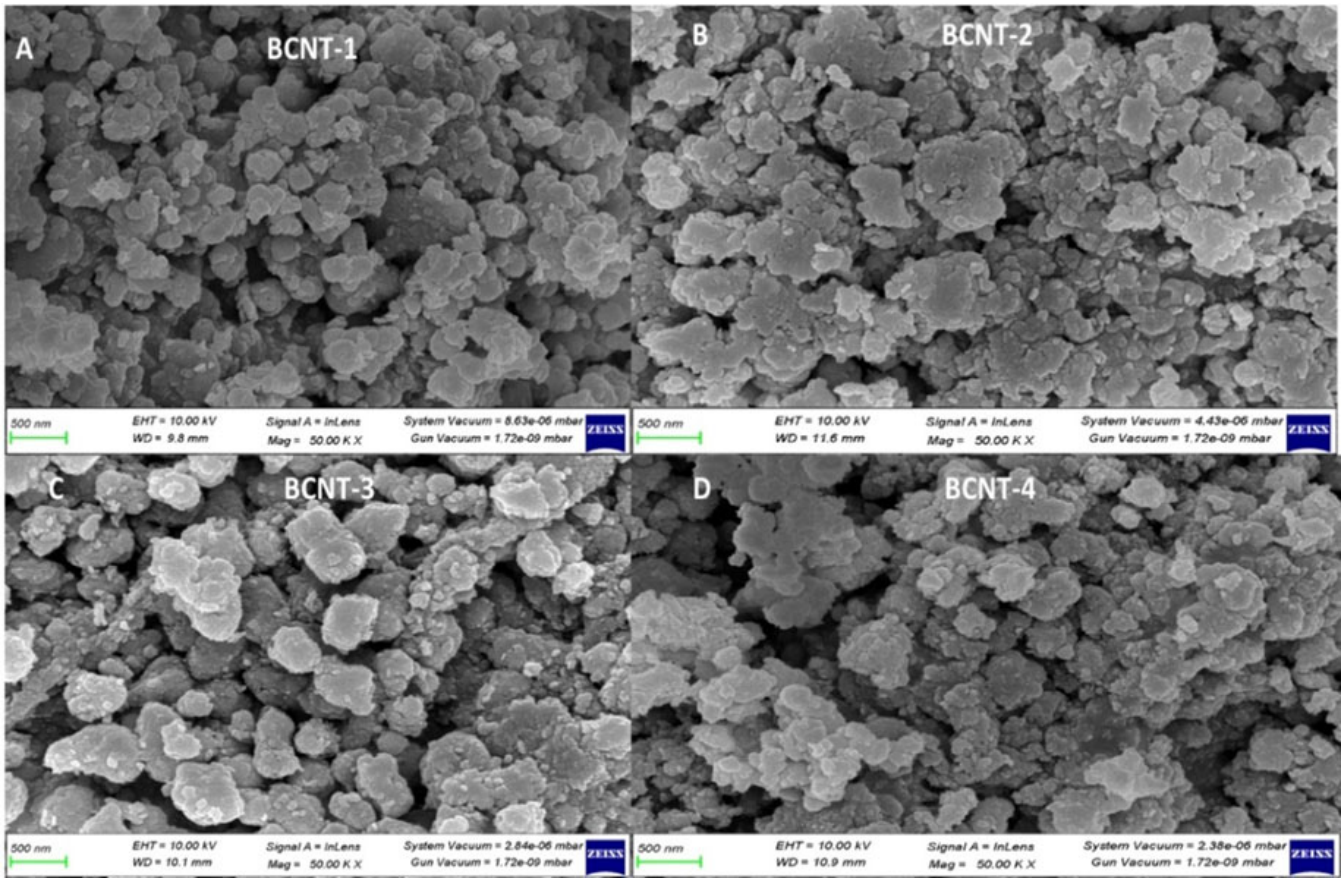

Fig. 2. FESEM images of $BaCuTiO_3$ doped $NiTiO_3$ nanocomposites (x = 0.2, 0.4, 0.6 and 0.8)

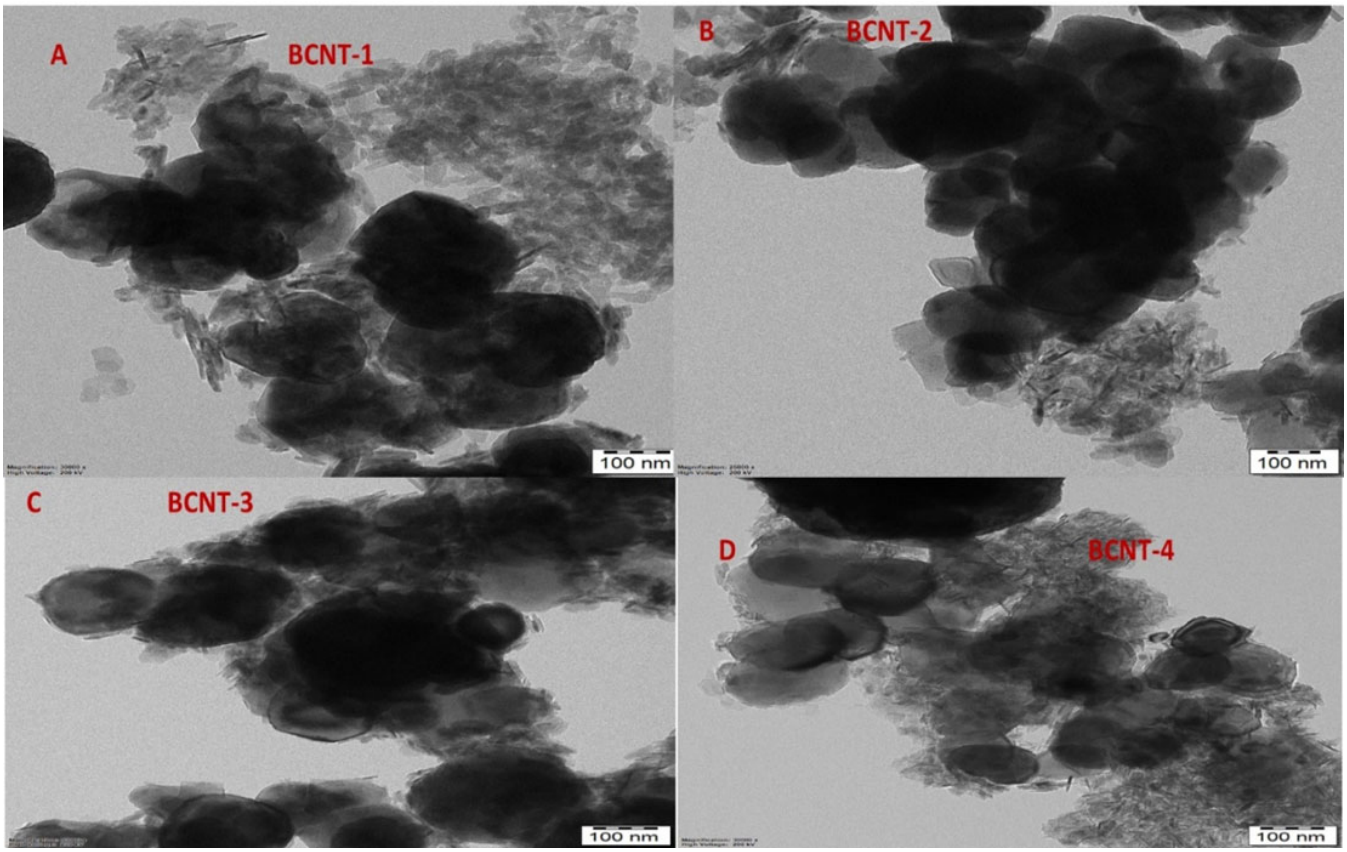

Fig. 3. TEM images of $BaCuTiO_3$ doped $NiTiO_3$ nanocomposites (x = 0.2, 0.4, 0.6 and 0.8)

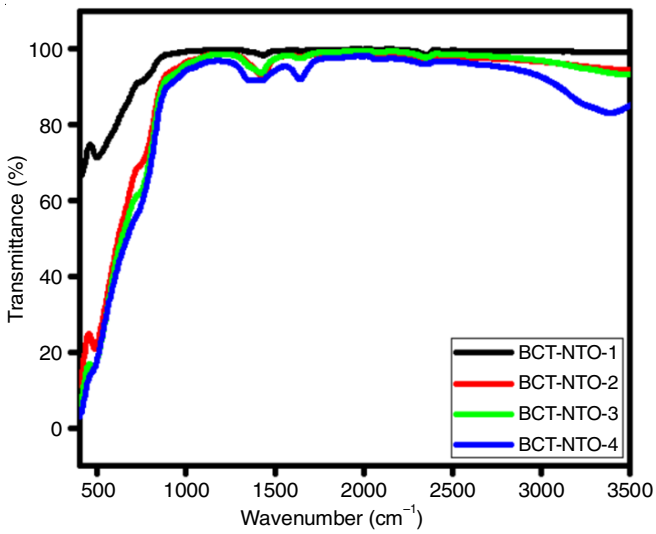

Fig. 4. FT-IR spectra of $BaCuTiO_3$ doped $NiTiO_3$ nanocomposites (x = 0.2, 0.4, 0.6 and 0.8)

Cu-O and Ti-O bonds is indicated by these two bands. Furthermore, the bending vibrations at 2353 cm^{-1} and 2457 cm^{-1} are due to the oxygen and hydrogen (O-H) transmittance of the BCT nanoparticles [14]. The intramolecular stretching modes that result from the unique hydrogen bonding features within the frame network of the perovskite structure, which are responsible for another affected peak, which is located at 3633 cm^{-1}. When metal ions are doped onto the surface of TiO_3, there is a noticeable shift in the absorption bands, along with the appearance of a new absorption band, signaling significant changes in the surface and electronic environment of TiO_3. The strong peaks observed around 466 cm^{-1}, corresponding to Ti-O stretching, clearly confirmed the formation of BCT-NTO nanocomposites (Table-2). This peak is particularly important as it directly verifies the successful incorporation of metal ions into the TiO_3 matrix, fundamentally altering its structural and electronic properties. These alterations underscore the influence of compositional variations on the bonding and structural characteristics of the composite. Significantly, at a concentration of 0.8, the overall intensity increases due to a broad C-O band, which predominantly affects the FTIR measurements.

TABLE-2
THE PEAK INTENSITY OF $BaCuTiO_3$ DOPED $NiTiO_3$ NANOCOMPOSITES (x = 0.2, 0.4, 0.6 and 0.8)

Sample	Peak	Intensity	Corr. intensity
BCT-NTO-1 (x = 0.2)	497.63	71.32	5.06
	2353.16	98.50	1.18
	3633.8	98.12	1.23
BCT-NTO-2 (x = 0.4)	489.92	20.93	7.28
	1427.32	92.92	5.59
	2457.31	97.97	0.12
	3861.49	96.26	0.11
BCT-NTO-3 (x = 0.6)	478.35	15.85	3.44
	1639.49	97.50	1.11
	2349.30	97.76	1.24
	3927.07	97.27	0.00
BCT-NTO-4 (x = 0.8)	1357.89	91.74	0.79
	1419.61	91.66	0.93
	1643.35	92.04	4.01
	3630.03	79.39	12.54

EDS studies: Elemental composition analysis using energy dispersive spectroscopy (EDS) confirmed the presence of oxygen, barium, copper, nickel and titanium, which are responsible for BCT-NTO nanocomposites fabrication. Fig. 5 depicts the EDS spectra of BCT-NTO nanocomposites consisting the elemental

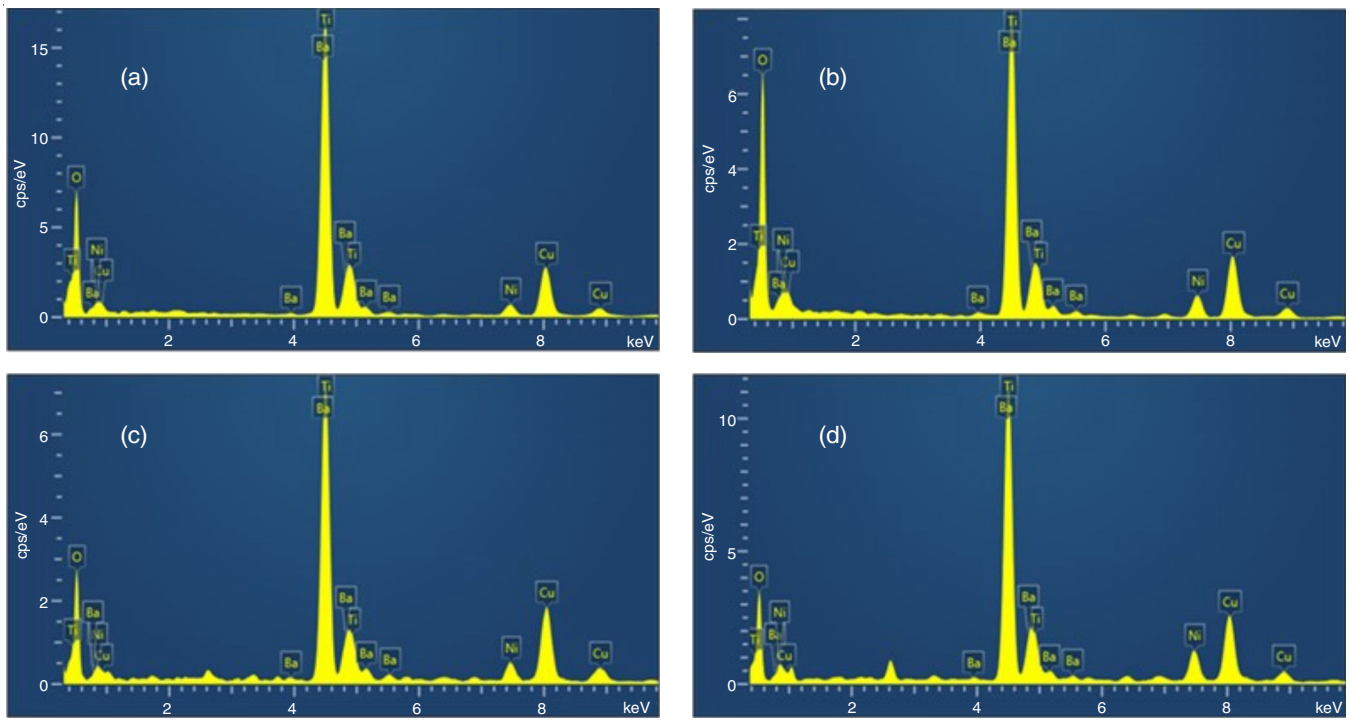

Fig. 5. EDS spectra of $BaCuTiO_3$ doped $NiTiO_3$ nanocomposites (x = 0.2, 0.4, 0.6 and 0.8)

composition of barium (Ba), copper (Cu), oxygen (O), nickel (Ni) and titanium (Ti) in the range of 700-780 nm [21]. Table-3 tabulates the BCT-NTO atomic and weight percentages.

As the nanocomposite concentration increases, EDS analysis reveals significant trends in the elemental distribution and composition that influence electrocatalytic performance. A more uniform distribution of key elements is observed, which is critical for maintaining consistent catalytic activity [22]. The stability of phases like $BaCuTiO_3$ and $NiTiO_3$ remains intact, indicating good compatibility between materials, which is vital for consistent performance. By examining these trends, the optimal $BaCuTiO_3$ to $NiTiO_3$ ratio can be determined to maximize the electrocatalytic activity, ensuring both efficiency and stability in applications such as energy harvesting or storage.

UV-visible studies: Using the DRS spectrum, the optical behaviour of the BCT-NTO/BCT-NTO nanocomposites was examined. The charge coordinated electronic transition between the O 2p state and the Ti at 3d state is indicated at 400 nm [23]. The colloidal fluid changes from white to a yellowish-grey colour during the synthesis process, signifying the formation of BCT-NTO nanocomposites shown in Fig. 6. The average crystalline size and the shift in the crystalline phase are correlated with the strong absorption peak [24]. The fabrication of BCT-NTO nanocomposites was confirmed by the prominent absorbance peak in the 385-400 nm.

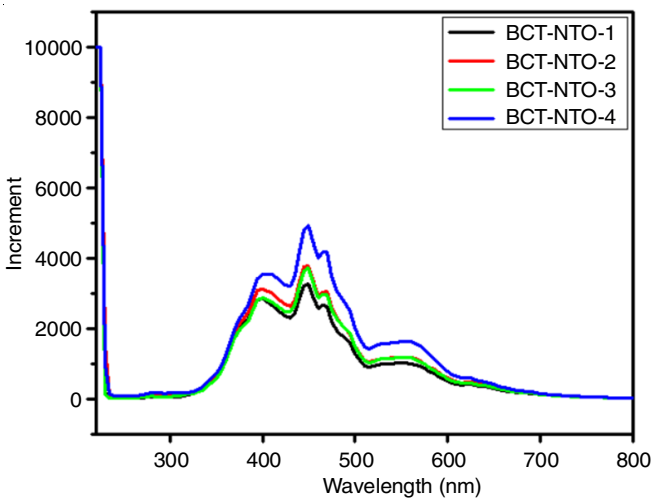

Fig. 6. UV-visible reflectance spectra of $BaCuTiO_3$ doped $NiTiO_3$ nanocomposites (x = 0.2, 0.4, 0.6 and 0.8)

XPS spectral studies: The XPS spectrum of BCT-NTO nanocomposite shown in Fig. 7 was recorded using high sensitivity mode with high photon energy (PE). This method enables the detection and analysis of elements present on the surface layer of the material, specifically those in amounts greater than 0.8 atomic percent (at.%). The full-range XPS survey spectrum (0 to 1400 eV) for BCT-NTO at x = 0.2 exhibited peaks corresponding to Ba, Ti, Ni, Cu and O, while the C 1s peak, due to surface carbon contamination, was used for calibrating the binding energies of other elements. All samples showed similar spectra, confirming the single-phase structure of the BCN-NTO, free from impurity phases.

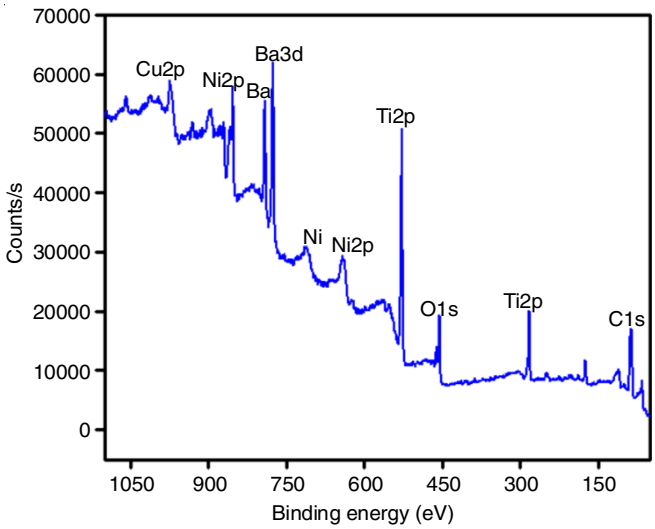

Fig. 7. XPS spectrum of $BaCuTiO_3$ doped $NiTiO_3$ nanocomposite (x = 0.2)

Barium carbonate ($BaCO_3$) at 780 eV in Ba 3d spectra, whereas at ~783 eV indicates the Ni2pBa phase, indicating a nickel-barium complex (NiBa). The Cu 2p peak reveals a high-energy doublet (primary peak at 936 eV) indicating Ti2pBaCu2p complex, which contains titanium, barium, copper and probably nickel. Low-energy doublet parameters at ~933.6 eV and ~942.5 eV confirmed the presence of copper oxide (Cu^{2+}). The Ti 2p spectra, at 295 eV, confirming the presence of Ti in the samples. The presence of Ni2pCu2pBa3d phase is confirmed by the Cu 2p spectra, suggesting a phase involving nickel, copper and barium. The Cu 2p signal from the Ba 3d phase may be specific to certain samples (IP), as indicated by the analysis of Ba 3d and Ti 2p peaks [25].

Despite changes in the concentration, oxygen vacancies remained consistent as the relative areas under the O peaks showed the minimal variation. These vacancies, often charged defects in nanocomposites, did not disrupt charge balance. The

TABLE-3
ELEMENTAL COMPOSITION of $BaCuTiO_3$ DOPED $NiTiO_3$ NANOCOMPOSITES

Elements	BCT-NTO-1 (x = 0.2)		BCT-NTO-2 (x = 0.4)		BCT-NTO-3 (x = 0.6)		BCT-NTO-4 (x = 0.8)	
	Weight (%)	Atomic (%)	Weight (%)	Atomic (%)	Weight (%)	Atomic (%)	Weight (%)	Atomic (%)
O	22.41	51.17	33.16	64.83	13.39	40.99	14.24	38.92
Ti	46.01	35.09	35.10	22.92	30.34	31.02	40.21	36.70
Ni	2.89	1.80	4.52	2.41	3.60	3.01	7.63	5.68
Cu	13.93	8.01	13.73	6.76	14.98	11.55	17.92	12.33
Ba	14.76	3.93	13.50	3.08	37.68	13.44	20.00	6.37
Total	100.00	100.00	100.00	100.00	100.00	100.00	100.00	100.00

findings from these spectra are consistent with XRD and FTIR analyses, providing further validation of the identified phases and compounds.

Magnetic behaviour: The magnetic behaviour and cationic redistribution effects observed in upon doping with Ba^{2+} ions. The magnetic behaviour analysis shows the magnetic behaviour of the BCT-NTO sample as indicated by the M-H loops (Fig. 8), a well-defined hysteresis loop with very small coercivity (H_c), remanence (M_r) and remanence ratio/saturation magnetization (M_s) (M_r/M_s), approaching zero. The small magnitude of these parameters suggests superparamagnetic behaviour, which can sometimes be influenced by environmental factors such as Earth's magnetic field or instrumental error.

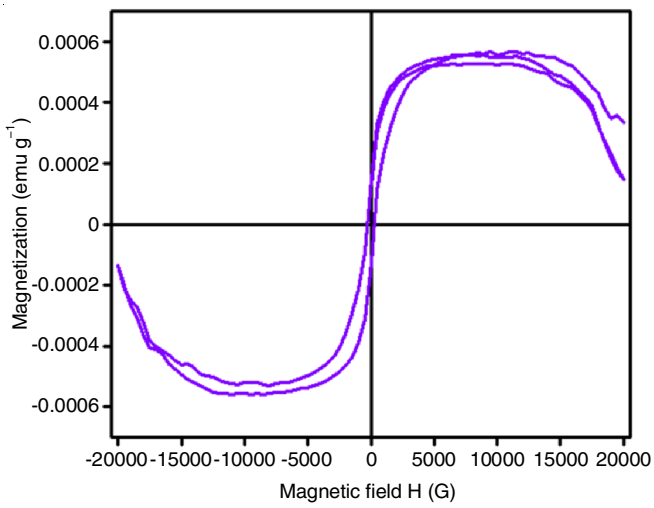

Fig. 8. M-H Loops of $BaCuTiO_3$ doped $NiTiO_3$ nanocomposite

The doping BCT-NTO sample with Ba^{2+} ions leads to a replacement of Cu^{2+} cations from the B-site (B-position) of the crystal lattice. The displaced Cu^{2+} cations are then shifted to the A-site (A-position). This doping process increases the concentration of Ba^{2+} cations, thereby allowing magnetic cations (such as Ni^{3+} originally at the B-site) to migrate towards the A-site. Consequently, the number of non-magnetic cations (Ba^{2+}) at the B-site increases. Generally, saturation magnetization (Ms) can depend on the types and arrangement of cations at the B-site within the crystal lattice. In case of Ba^{2+} ion doping in BCT-NTO, the movement of magnetic cations (Ni^{3+} from B-site to A-site) away from the B-site decreases the magnetic exchange interactions between A and B-sites. This redistribution of cations and subsequent decrease in magnetic exchange interactions contribute to the observed superparamagnetic behaviour and altered magnetic properties of the BCT-NTO sample. The magnetic exchange interactions between A and B-sites can be modeled using a two-sublattice model, taking into account the distribution of different cation types across the crystal lattice. The experimental measurement of magnetic moment (n_B) in BCT-NTO nanocomposite reflects the difference in magnetic moments between B and A-sites (M_B - M_A), illustrating the impact of cationic redistribution on the magnetic behaviour [26,27]. In summary, the doping of Ba^{2+} ions into BCT-NTO induces significant changes in cation distribution within the crystal lattice, leading to altered magnetic properties characterized by superparamagnetic behaviour and reduced magnetic exchange interactions between different cation sites (A and B-sites). This analysis highlights the intricate relationship between cationic composition and magnetic behaviour in doped oxide materials like BCT-NTO.

Cyclic voltammetry (CV) analysis: For cyclic voltammetry study in 1 M aq. KOH electrolyte in a three-electrode setup, platinum foil has been used as the counter electrode and Ni/$NiTiO_3$ as the reference electrode in the current work. BCT-NTO in 2 M KOH, BCT-NTO in 2 M NaOH and BCT-NTO in 2 M $BaNO_3$ are all active electrochemical materials which generate workable electrodes. Comparing BCT-NTO in NaOH electrolyte to BCT-NTO in $BaNO_3$, the region covered by BCT-NTO in NaOH electrolyte is larger at a scan rate of 10 mV/s and nearly identical to that of KOH electrolyte. Since specific capacitance depends on the region covered by the CV curve and is exactly proportional to the specific capacitance. The BCT-NTO electrode material in NaOH has the highest specific capacitance value, according to the CV analysis. The substantial specific surface area structures have the potential to enhance the ion adsorption efficiency and double-layer capacitance due to their larger surface area and high surface-to-volume ratio at the nanoscale. Subsequently, as illustrated in Fig. 9a-d, the BCT-NTOs CV value was evaluated at different scan rates (10-90 mV/s). The absence of symmetry in the CV curves supports the pseudo-capacitance behaviour of the electrode material [28].

Fig. 10 shows the galvanostatic charging discharging (GCD) plots at various concentrations for BCT-NTO composites having a non-linear curve with a typical redox active behaviour. The charge/discharge duration was observed to decrease with increase in current density ascribed to increase of potential drop and inadequate Faradaic reactions at higher scan rates. The extraordinary symmetric GCD profile of BCT-NTO nanocomposite electrodes in the potential range of 10 mA to 70 mA for current densities of BCT-NTO ($x = 0.2$-0.8) (Fig. 11a-d) shows that a voltage plateau demonstrates around 0.27 V during the charge cycle and between 0.02 and 0.005 V during the discharge cycle, confirming the presence of a pseudocapacitive reaction during the charge/discharge processes.This behaviour is in perfect agreement with CV profiles [29-32] and indicates the exceptionally reversibility during the charge/discharge processes. Moreover, similar charge and discharge times show that the redox reaction is highly reversible.

The GCD cycles of the BCT-NTO electrode are displayed in Fig. 12a-d at different current densities between 10 mV and 70 mV in the potential range between -0.1 and 0.3 V. In this case, every GCD profile also showed the distinct potential plateau areas with characteristics specific to the kind of battery which indicated an exceptional pseudocapacitive behaviour. Similarly, every GCD profile also showed exceptionally reversible charge-discharge characteristics and nearly symmetric charge-discharge patterns (Fig. 13a-d), demonstrating the exceptional capacitive qualities and better reversibility of the redox reaction. The discharge components of the GCD curves were used to determine specific capacitance and the resulting capaci-

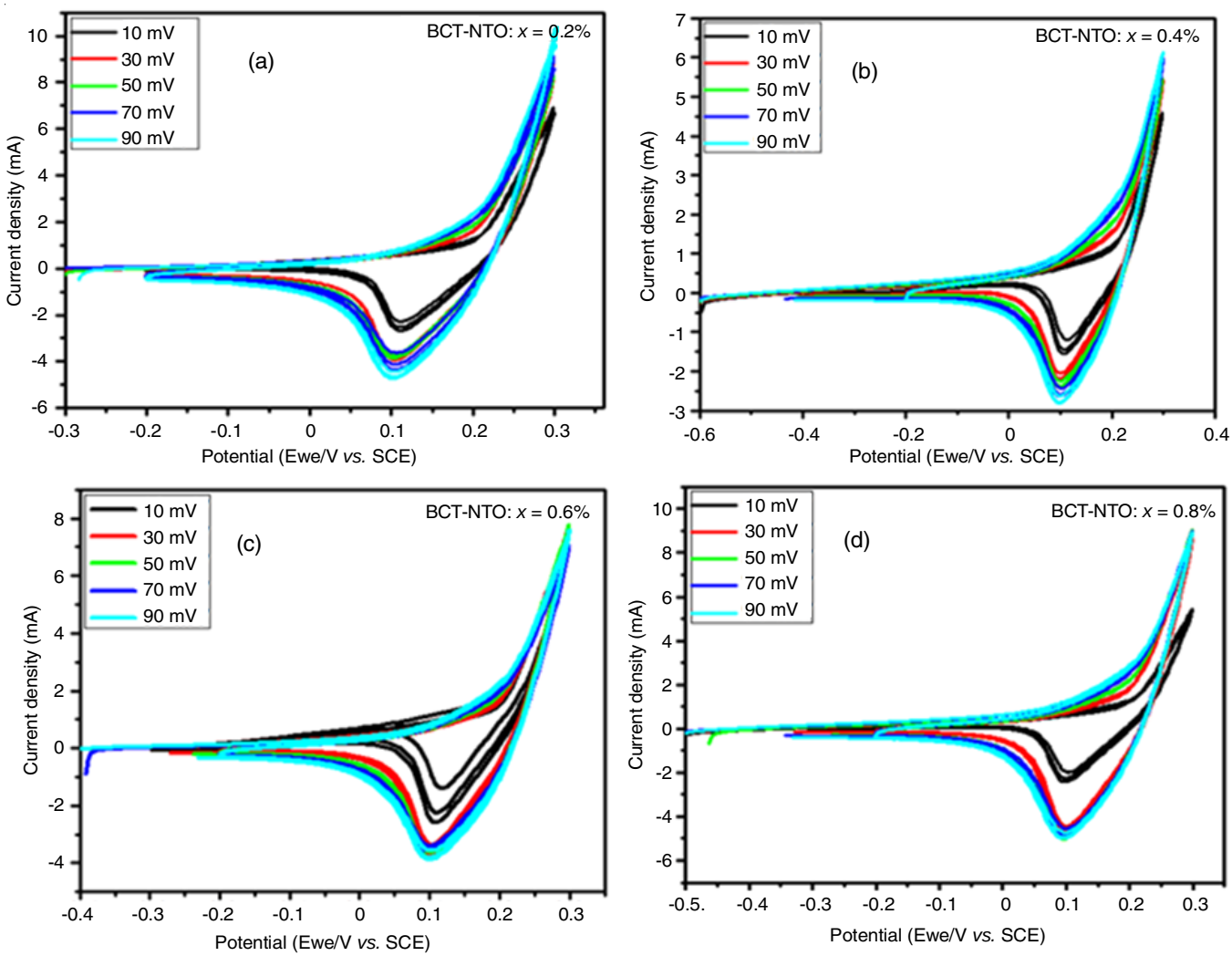

Fig. 9(a-d). Cyclic voltamograms of $BaCuTiO_3$ doped $NiTiO_3$ nanocomposites (x = 0.2, 0.4, 0.6 and 0.8) at 10 mV/s to 90 mV/s scan rate in electrolyte method

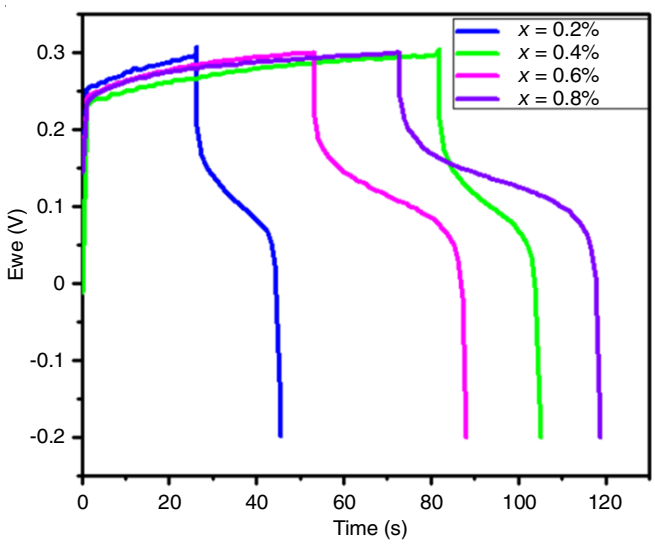

Fig. 10. GCD plots of $BaCuTiO_3$ doped $NiTiO_3$ nanocomposites (x = 0.2, 0.4, 0.6 and 0.8)

tances at various current densities [25-27]. The charging and discharging cycles of nanocomposite samples demonstrate a remarkable stability over 350 cycles and also stable with different current, power and charge with respect to time period. This confirms the excellent storage stability and long-term durability of the samples.

Conclusion

A synthesis of nanostructured $Ba_{0.8}Cu_{0.2}TiO_3$-$NiTiO_3$ (BCT-NTO) nanocomposites through a hydrothermal process, with films fabricated using the spin coating technique was successfully achieved. Structural and morphological analyses using TEM, SEM, FTIR and XRD techniques confirmed the fabrication of BCT-NTO nanoparticles, with sizes ranging from 8 to 32 nm and a band gap of 3.6 eV. These results affirm that the synthesized BCT-NTO nanocomposite exhibits desirable characteristics for piezoelectric energy harvesting applications. The use of the piezoelectric effect in these nanocomposites underscores their potential in converting mechanical stress into electrical energy, making them suitable for integration into the modern self-powered devices. The successful synthesis of BCT-NTO nanoparticles, characterized by their structural and optical properties, highlights their high compatibility and effectiveness as functional materials for energy harvesting. The

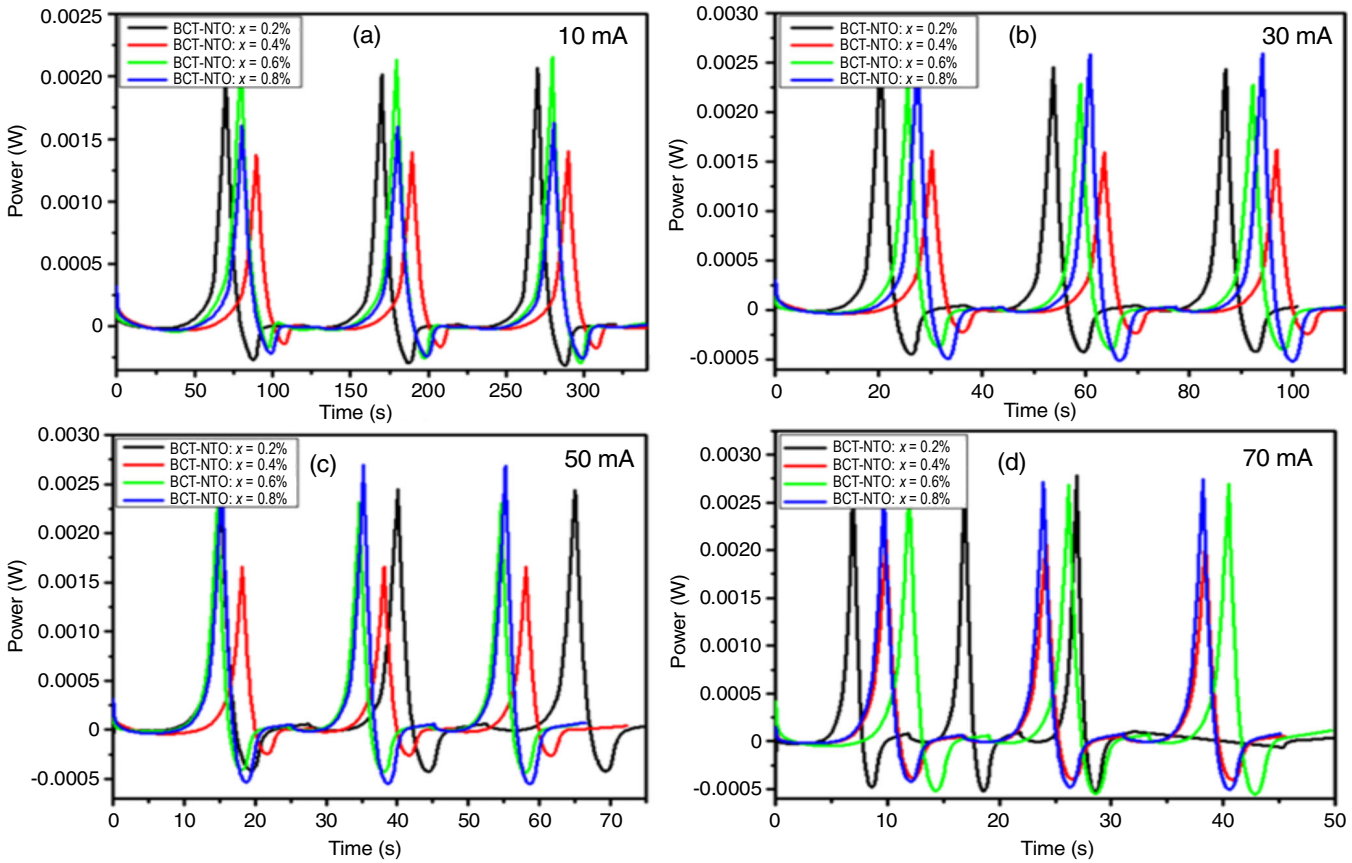

Fig. 11a-d. GCD curves (time-power) of $BaCuTiO_3$ doped $NiTiO_3$ nanocomposites (x = 0.2, 0.4, 0.6 and 0.8) at different current values

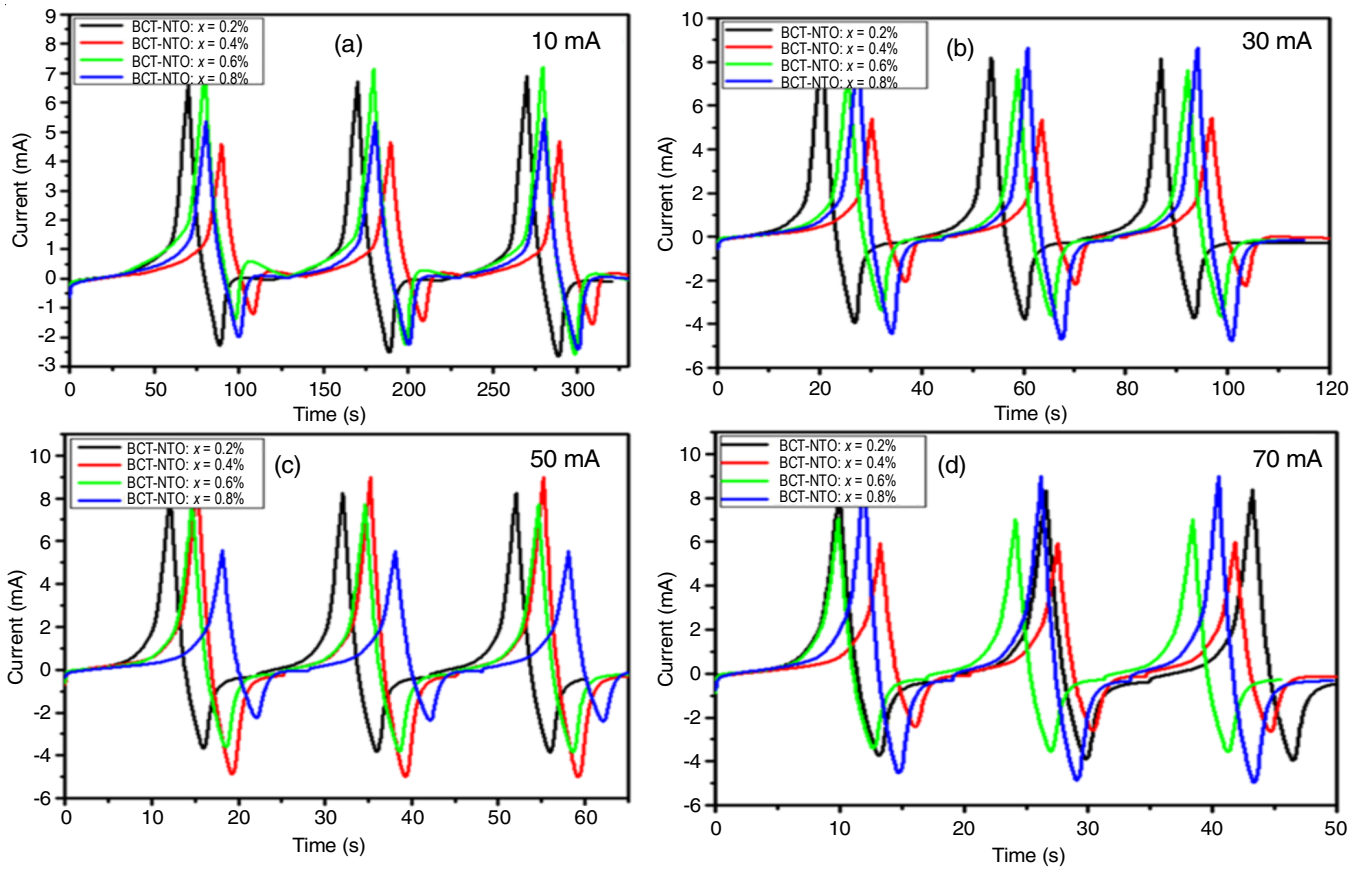

Fig. 12a-d. GCD curves (time *vs.* current) of $BaCuTiO_3$ doped $NiTiO_3$ nanocomposites (x = 0.2, 0.4, 0.6 and 0.8) at scan rates of 10-70 mV

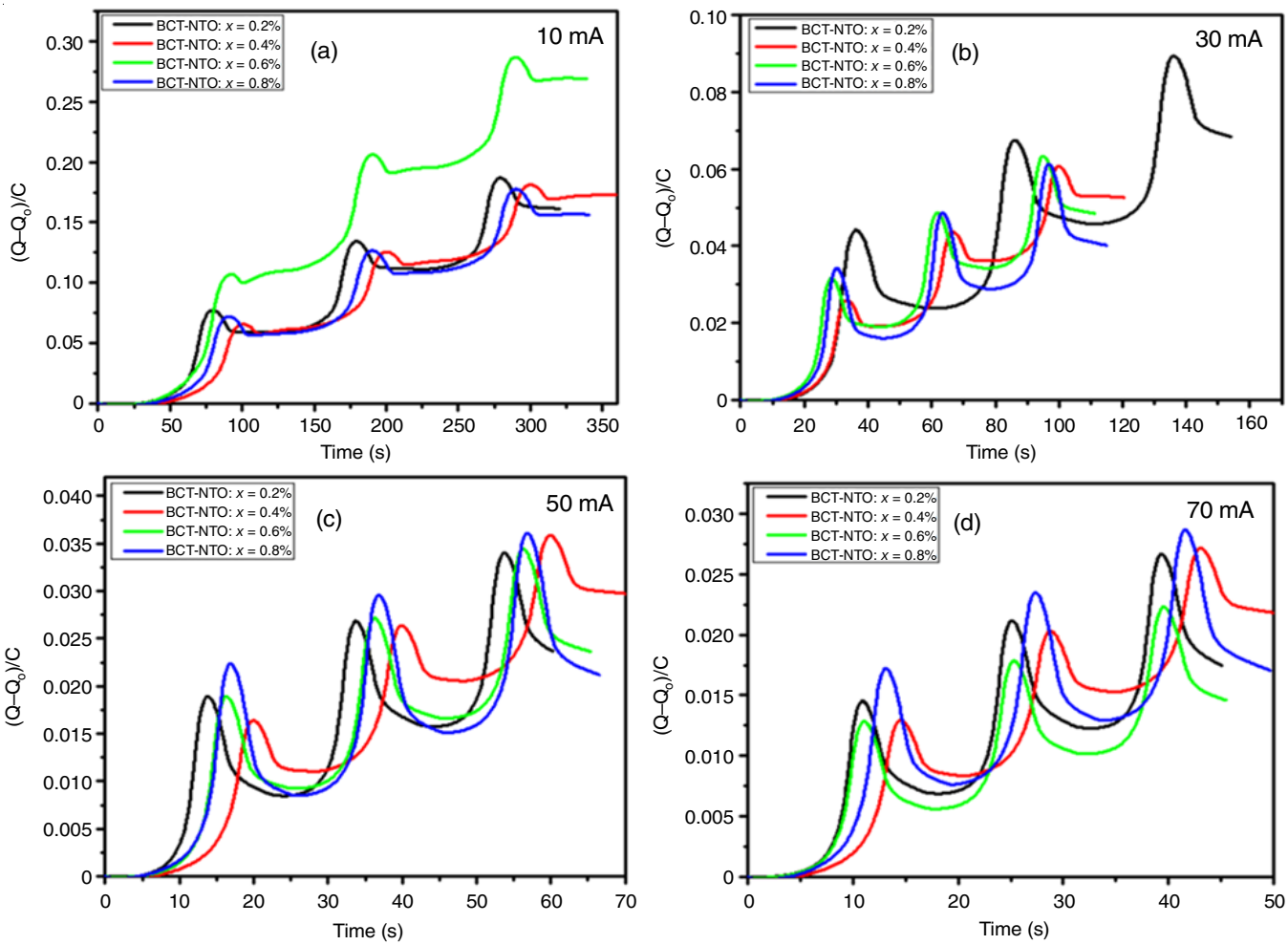

Fig. 13a-d. GCD curves (time *vs.* charge) of $BaCuTiO_3$ doped $NiTiO_3$ nanocomposites (x = 0.2, 0.4, 0.6 and 0.8) at scan rates of 10-70 mV

BCT-NTO nanocomposite shows great promise for various applications, making piezoelectric nanogenerators a key future option for low-power, autonomous devices. CV provides useful applications in energy storage and conversion for lithium-ion batteries, fuel cells, supercapacitors and more, while also being widely used in fields like materials science, photonics, biology and chemistry.

ACKNOWLEDGEMENTS

The authors are grateful to the Mangement, ASK Analytical Services, Bangaluru, India for the constant support in the characterization and measurements of the materials.

CONFLICT OF INTEREST

The authors declare that there is no conflict of interests regarding the publication of this article.

REFERENCES

1. K. Uchino, *Energy Technol.*, **6**, 829 (2018); https://doi.org/10.1002/ente.201700785
2. X. Wang, *Nano Energy*, **1**, 13 (2012); https://doi.org/10.1016/j.nanoen.2011.09.001
3. C.R. Bowen, H.A. Kim, P.M. Weaver and S. Dunn, *Energy Environ. Sci.*, **7**, 25 (2014); https://doi.org/10.1039/C3EE42454E
4. H. Li, C. Tian and Z.D. Deng, *Appl. Phys. Rev.*, **1**, 041301 (2014); https://doi.org/10.1063/1.4900845
5. H.A. Sodano, D.J. Inman and G. Park, *Shock Vibration Digest*, **36**, 197 (2004); https://doi.org/10.1177/0583102404043275
6. C. Wan and C.R. Bowen, *J. Mater. Chem. A Mater. Energy Sustain.*, **5**, 3091 (2017); https://doi.org/10.1039/C6TA09590A
7. B. Maamer, A. Boughamoura, A.M.R. Fath El-Bab, L.A. Francis and F. Tounsi, *Energy Convers. Manage.*, **199**, 111973 (2019); https://doi.org/10.1016/j.enconman.2019.111973
8. G. Piliposian, A. Hasanyan and D. Piliposyan, *J. Phys. D Appl. Phys.*, **52**, 445501 (2019); https://doi.org/10.1088/1361-6463/ab37be
9. M.B. Gawande, A. Goswami, F.-X. Felpin, T. Asefa, X. Huang, R. Silva, X. Zou, R. Zboril and R.S. Varma, *Chem. Rev.*, **116**, 3722 (2016); https://doi.org/10.1021/acs.chemrev.5b00482
10. G. Oberdörster, A. Maynard, K. Donaldson, V. Castranova, J. Fitzpatrick, K. Ausman, J. Carter, W. Kreyling, D. Lai, S. Olin, N. Monteiro-Riviere, B. Karn, D. Warheit and H. Yang, *Part. Fibre Toxicol.*, **2**, 8 (2005); https://doi.org/10.1186/1743-8977-2-8
11. A. Bezryadin, A. Belkin, E. Ilin, M. Pak, E.V. Colla and A. Hubler, *Nanotechnology*, **28**, 495401 (2017); https://doi.org/10.1088/1361-6528/aa935c
12. X. Hao, *J. Adv. Dielectr.*, **03**, 1330001 (2013); https://doi.org/10.1142/S2010135X13300016
13. B. Chu, X. Zhou, K. Ren, B. Neese, M. Lin, Q. Wang, F. Bauer and Q.M. Zhang, *Science*, **313**, 334 (2006); https://doi.org/10.1126/science.1127798

14. Z.M. Dang, J.K. Yuan, S.H. Yao and R.J. Liao, *Adv. Mater.*, **25**, 6334 (2013); https://doi.org/10.1002/adma.201301752
15. Q. Li, G. Zhang, F. Liu, K. Han, M.R. Gadinski, C. Xiong and Q. Wang, *Energy Environ. Sci.*, **8**, 922 (2015); https://doi.org/10.1039/C4EE02962C
16. A. Awadallah-F and S. Al-Muhtaseb, *Sci. Rep.*, **10**, 4878 (2020); https://doi.org/10.1038/s41598-020-61726-4
17. B.D. Cullity, Elements of X-ray diffraction, Addison-Wesley Publishing Com-pany Inc, London, p. 99 (1978).
18. K. Chandra Babu Naidu, *Mater. Res. Bull.*, **89**, 125 (2017); https://doi.org/10.1016/j.materresbull.2017.01.015
19. K. Chandra Babu Naidu, S. Roopas Kiran and W. Madhuri, *IEEE Trans. Magn.*, **53**, 1 (2017); https://doi.org/10.1109/TMAG.2016.2625773
20. K. Chandra Babu Naidu and W. Madhuri, *Mater. Chem. Phys.*, **187**, 164 (2017); https://doi.org/10.1016/j.matchemphys.2016.11.062
21. G. Venkatesh, M. Geerthana, S. Prabhu, R. Ramesh and K.M. Prabu, *Optik (Stuttg.)*, **206**, 164055 (2020); https://doi.org/10.1016/j.ijleo.2019.164055
22. D. Zhao, Y. Gao, L. Yang, Y. Chen, Y. Wang, Q. Zheng, K.-H. Lam and D. Lin, *Ceram. Int.*, **50B**, 2350 (2024); https://doi.org/10.1016/j.ceramint.2023.11.013
23. B. Choudhury, M. Dey and Choudhury, *Int. Nano Lett.*, **3**, 25 (2013); https://doi.org/10.1186/2228-5326-3-25
24. S.T. Fardood, A. Ramazani, Z. Golfar and S.W. Joo, *J. Appl. Chem. Res.*, **11**, 19 (2017).
25. A.V. Fetisov, G.A. Kozhina, S.Kh. Estemirova, V.B. Fetisov, V.Ya. Mitrofanov, S.A. Uporov and L.B. Vedmid, *J. Spectrosc.*, **2013**, 217268 (2013); https://doi.org/10.1155/2013/217268
26. U. Naresh, R.J. Kumar and K.C.B. Naidu, *Mater. Chem. Phys.*, **236**, 121807 (2019); https://doi.org/10.1016/j.matchemphys.2019.121807
27. A. Rani, J. Kolte and P. Gopalan, *Ceram. Int.*, **41**, 14057 (2015); https://doi.org/10.1016/j.ceramint.2015.07.023
28. C.K. Maity, G. Hatui, S. Sahoo, P. Saren and G.C. Nayak, *ChemistrySelect*, **4**, 3672 (2019); https://doi.org/10.1002/slct.201803560
29. J. Zhang, F. Liu, J. Cheng and X. Zhang, *ACS Appl. Mater. Interfaces*, **7**, 17630 (2015); https://doi.org/10.1021/acsami.5b04463
30. B. Abdolahi, M.B. Gholivand, M. Shamsipur and M. Amiri, *Int. J. Energy Res.*, **45**, 12879 (2021); https://doi.org/10.1002/er.6618
31. P. Bandyopadhyay, G. Saeed, N.H. Kim and J.H. Lee, *Chem. Eng. J.*, **384**, 123357 (2020); https://doi.org/10.1016/j.cej.2019.123357
32. A.W. Anwar, A. Majeed, N. Iqbal, W. Ullah, A. Shuaib, U. Ilyas, F. Bibi and H.M. Rafique, *J. Mater. Sci. Technol.*, **31**, 699 (2015); https://doi.org/10.1016/j.jmst.2014.12.012